Chemical Engineering Journal 477 (2023) 147141

Contents lists available at ScienceDirect

Chemical Engineering Journal

journal homepage: www.elsevier.com/locate/cej

CO_2-mediated porphyrin catalysis in reversible Li-CO_2 cells

Boran Kim [a,1], Kihyun Shin [b,c,1], Graeme Henkelman [b], Won-Hee Ryu [a,*]

[a] Department of Chemical and Biological Engineering, Sookmyung Women's University, 100 Cheongpa-ro 47-gil, Yongsan-gu, Seoul 04310, Republic of Korea
[b] Department of Chemistry and the Oden Institute of Computational Engineering and Sciences, University of Texas at Austin, Austin, TX 78712, United States
[c] Department of Materials Science and Engineering, Hanbat National University, Daejeon 34158, Republic of Korea

A B S T R A C T

Li-CO_2 cells provide exceptional benefit by storing considerable energy and achieving environmental carbon fixation. However, the sluggish kinetics of the Li-CO_2 reaction and severe cell polarization with low efficiency must be addressed. Here, we show that the manganese phthalocyanine (MnPc) molecule, a porphyrin-based homogeneous catalyst, significantly reduces the overpotential (~50 %) and improves Li-CO_2 cell performance during prolonged cycling. The reversible Li-CO_2 reaction pathway proceeding via a Li_xCO_2 intermediate species and catalyzed by MnPc was examined by *in situ* characterization and first principles calculations. We reveal the structural changes occurring in the MnPc catalyst with metal-to-ligand charge transfer when the electrochemically reduced CO_2^{*-} radical intermediate is bound to the Mn center after discharge; consequently, the reverse reaction enables recharging. This study introduces a way to understand and design organometallic homogeneous catalysts involving CO_2 mediation of environmental energy storage systems and carbon negative.

1. Introduction

Excessive greenhouse gas (e.g., CO_2) emissions arising from industry and vehicles and consequent global warming have been recognized as leading to a forthcoming crisis. Tremendous effort has been expended to develop electrochemical energy conversion and storage systems to mitigate our carbon footprint[1–11]. Li-CO_2 cells have been highlighted for electrochemical CO_2 reduction and utilization due to their combined benefits of energy storage and environmental CO_2 fixation[12–19]. Li-CO_2 cells with a Li metal anode and gaseous CO_2 cathode undergo electrochemical storage reactions with atmospheric CO_2 pollutants and spontaneously produce electrical energy. The cathodic reaction based on transition metal-free and lightweight CO_2 (M_w = 44) delivers a high theoretical energy density of 1,876 Wh kg^{-1} [17,20–25]. The cathodic reaction between Li^+ and CO_2 involves the reversible formation and decomposition of lithium carbonate ($4Li^+ + 3CO_2 + 4e^- \rightarrow 2Li_2CO_3 + C$, ($E_o$ = 2.80 V versus Li/Li^+) on the cathodic electrode [26–33]. Nevertheless, because the discharged product species (i.e., Li_2CO_3) are thermodynamically stable and electrically insulating, a considerable portion of the product often remains even after reverse charging, resulting in low efficiency and poor reversibility [17,34,35]. Catalyst materials have been on the cathodic electrode to expedite Li-CO_2 reactions, yet unwanted covering and deactivation of catalysts on the electrode by discharged products should be addressed.

To solve this problem, homogeneous catalysts for Li-CO_2 batteries have been introduced, inspired from those of Li-O_2 batteries. The utilization of homogeneous catalyst called redox mediator (RM) dissolved in an electrolyte is an alternative route for catalyzing the Li-CO_2 reaction without catalyst deactivation [36–44]. Moreover, the RM provides a reversible redox switch that couples with the electrochemistry of Li_2CO_3 and provides an electrochemical path to lower the overpotential of the Li-CO_2 battery by directly transferring electrons instead of slow diffusion through insulating products. Since redox mediators act as mobile catalysts in the electrolyte, reactions at solid–liquid interfaces can occur much more easily, compared to the large overpotential that occurs in solid–solid reactions. Among various possible candidates, metal phthalocyanines, a family of organometallic porphyrin molecules, are based on benzene-containing organic compounds and contain an open axial coordination site that can actively bind CO_2. Their aromatic structures allow electron resonance in the porphyrin ring, thereby facilitating electron withdrawal or donation from/to intermediate reaction species (e.g., CO_2^{*-} radicals), thus enhancing the kinetics of CO_2 reduction and evolution.

In this work, we present dual functions of Mn phthalocyanine (MnPc) molecules serving as electrolyte catalysts coordinating CO_2^{*-} radical anions to produce high efficiency and reversibility in Li-CO_2 cells. As illustrated in Fig. 1. MnPc catalysts mediate charge transfer by binding with electrochemically reduced CO_2^{*-} radical anions during discharge and consequently promote a reaction sequence in which Li_2CO_3 and C products are formed and reversibly evolved. The electrochemical

* Corresponding author.
E-mail address: whryu@sookmyung.ac.kr (W.-H. Ryu).
[1] These authors contributed equally to this work.

https://doi.org/10.1016/j.cej.2023.147141
Received 25 June 2023; Received in revised form 16 October 2023; Accepted 2 November 2023
Available online 4 November 2023

properties of Li-CO_2 cells employing MnPc catalysts are evaluated to verify the catalysis of CO_2 fixation and evolution. The reversibility and products of Li-CO_2 cells with MnPc are investigated with *ex situ* characterization. The MnPc-mediated reaction mechanisms of Li-CO_2 cells are also verified by determining the Gibbs free energies of all intermediate species and conducting *in situ* differential electrochemical mass spectrometry (DEMS) analyses. We further elucidate the structural and chemical changes of the MnPc catalyst itself during Li-CO_2 reactions by observing reversible charge transfer and CO_2 binding processes through real-time spectroelectrochemical analyses during cycling. We successfully confirmed the characteristics of CO_2^{*-} radical anion adsorption and the redistribution of transferred electron density in the MnPc molecule by simulating the absorption spectra with time-dependent Hartree-Fock (TDHF) calculations and performing charge transfer analyses.

2. Results and Discussion

We incorporated MnPc into the Li-CO_2 cell as a porphyrin-based electrolyte catalyst to promote the reaction kinetics and evaluated the electrochemical performance (Fig. 2). To determine electrochemical redox information, we performed cyclic voltammetry (CV) studies on Li-CO_2 cells under Ar and CO_2 atmospheres without or with MnPc (Fig. 2**a and b**). In an inert atmosphere (Ar-purged), the cell exhibited a negligible electrochemical signal without redox peaks, whereas in a CO_2 atmosphere, the Li ions electrochemically reacted with CO_2 ($4Li^+ + 3CO_2 + 4e^- \leftrightarrow 2Li_2CO_3 + C$) to increase the current in the cathodic and anodic regions (Fig. 2**a**). In the case of Li-CO_2 cells containing MnPc, the onset potentials of the CO_2-purged cells were 2.75 V for the CO_2 reduction reaction (CRR) and 3.6 V for the CO_2 evolution reaction (CER) regardless of the purging environment, which indicated the intrinsic redox reactions of MnPc in the cells (Fig. 2**b**). The currents of the cathodic redox peaks were reinforced in the case of CO_2-purged cells, which implied the operation of a CO_2-mediated reaction. The potential difference between the onset potentials of the CRR (3.0 V) and CER (3.5 V) provided a low overpotential of 0.5 V for the Li-CO_2 cell containing MnPc compared to 0.85 V for the Li-CO_2 cell without MnPc, indicating the enhanced reversibility for both discharge and charging reactions provided by the MnPc catalysts (Fig. 2**c**). The additional peak at 2.8 V in the cathodic region was related to reduction reaction ($4Li^+ + 3CO_2 + 4e^- \rightarrow 2Li_2CO_3 + C$) accelerated by the MnPc catalyst. The peak intensity at this position (2.8 V) is higher when MnPc is used because the reaction is accelerated by MnPc and the reaction amount of the reduction reaction increases. In the anodic region, the CO_2 evolution reaction was significantly catalyzed and showed a higher current past 3.5 V than the pristine system. Fig. 2**d and e** presents the 1st discharge/charge curves with capacity limits of 500 mAh/g to compare the Li-CO_2 cells without and with MnPc. The Li-CO_2 cell without MnPc showed a highly polarized profile with a substantial overpotential of 1.8 V at the beginning of the charging process (Fig. 2**d**). On the other hand, the cell with the MnPc catalyst exhibited a significantly reduced overpotential of 0.9 V, resulting in charge polarization reduction (Fig. 2**e and f**). The charge–discharge profiles and the reduced overpotential remained stable during repeated cycling (Fig. 2**e**). To investigate the effects of the MnPc-mediated redox process on the full capacity, Fig. 2**g** shows full charge–discharge curves with MnPc under Ar and CO_2 atmospheres. The cell purged with Ar exhibited a very low discharge/charge capacity of 121 mAh/g. In contrast, during purging with CO_2, the cell delivered a high discharge capacity of 4,765 mAh/g and a reverse charge capacity of 3,560 mAh/g; this represents improved full capacity, even compared with pristine Li-CO_2 cells (1,825 mAh/g for discharge, 1,797 mAh/g for charge) (Fig. 2**g and Figure S1**). Most RMs are directly reduced or oxidized, thereby exhibiting capacity in the cell instead of direct Li-CO_2 reaction. Interestingly, the capacity with MnPc alone was negligible for the Ar-purged cell, implying that MnPc does not transfer electrons for redox reactions, unlike other classes of RMs, and tends instead to adsorb or desorb CO_2^{*-} radical anions. Therefore, the MnPc catalysts in the cell were particularly active for coordination of CO_2 intermediate species rather than for direct redox reactions. We also examined the cycling performance of Li-CO_2 cells with MnPc catalysts and a limited capacity of 500 mAh/g (Fig. 2**h**). The capacity of the MnPc-containing Li-CO_2 cell was stably maintained for more than 80 cycles, whereas the capacity of the pristine Li-CO_2 cell was gradually degraded before 35 cycles,

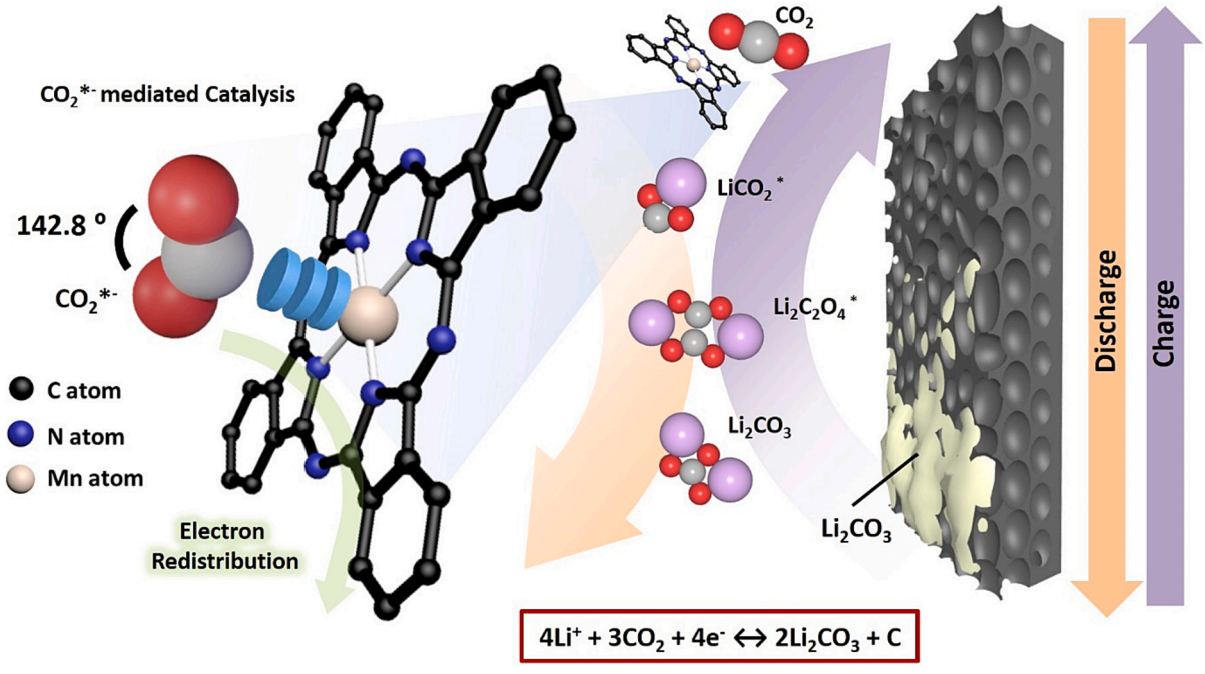

Fig. 1. Schematic illustration of the oxygen electrode in a MnPc-containing Li-CO_2 battery system. The proposed mechanism for the MnPc-containing Li-CO_2 battery was consistent with our analysis. During discharge, the Mn atom located in the center of phthalocyanine combined with the electrochemically reduced CO_2 to stabilize the radical ion by electron redistribution within the structure. As a result, MnPc promoted electron transfer to improve the reaction kinetics, thereby exhibiting a catalytic effect.

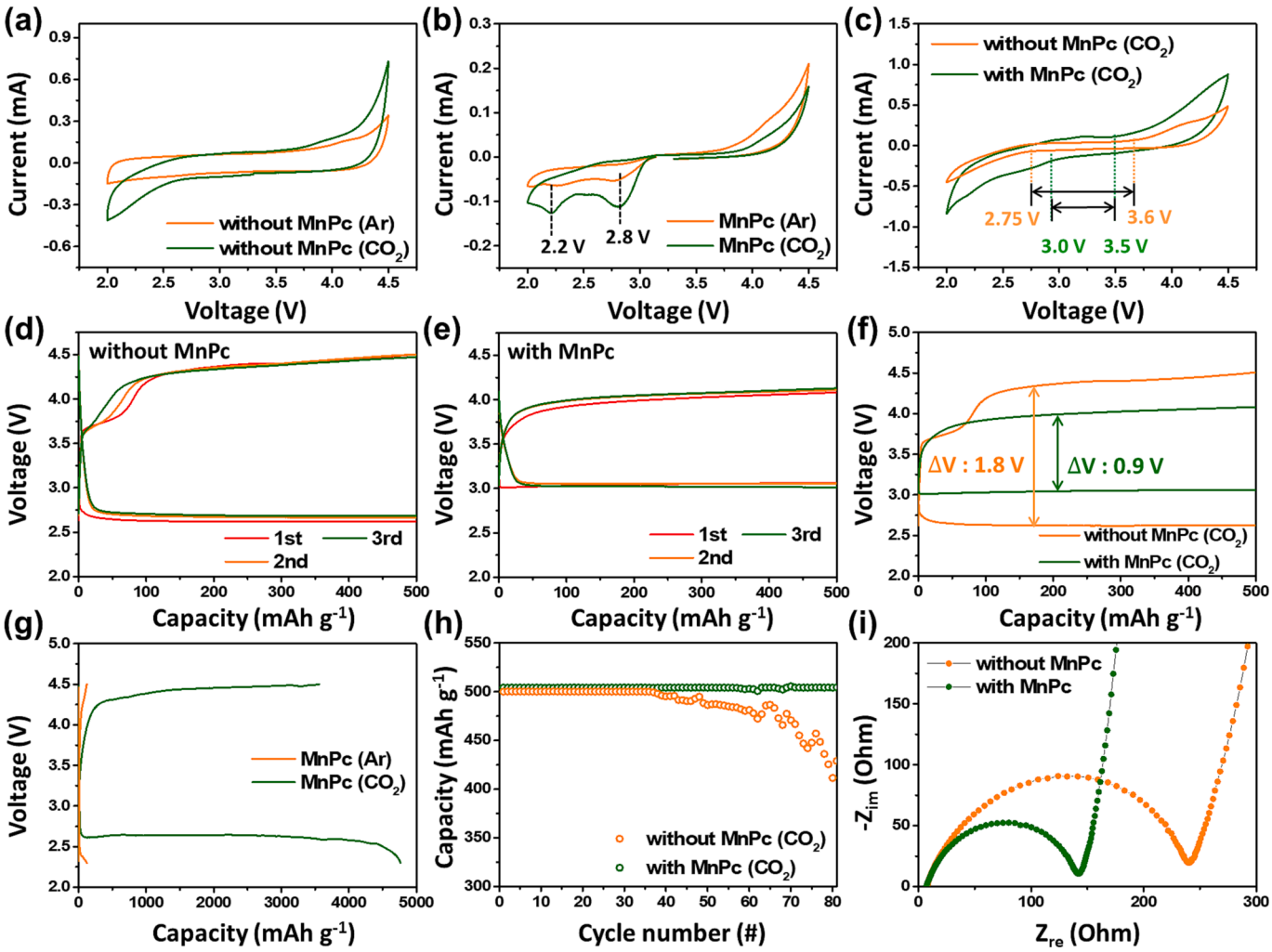

Fig. 2. Li-CO_2 cell performance with the MnPc-containing electrolyte. Cyclic voltammetry (CV) curves generated with a scan rate of 0.1 mVs^{-1} for Li-CO_2 with electrolytes containing 1 M LiFTSI + TEGDME (a) and 1 M LiTFSI + TEGDME + MnPc (b) after purging with Ar and CO_2. c, CV curves for Li-CO_2 cells with and without MnPc in LiTFSI + TEGDME solutions. d, e, Cycling behaviors of Li-CO_2 batteries without MnPc (d) and with MnPc (e) in the electrolyte, measured at 50 mA g^{-1} carbon with a limited capacity of 500 mAh/g carbon. f, Discharge–charge curves of the first cycles measured over the window 2.3–4.5 V for Li–CO_2 cells. g, Initial charge/discharge curves of the MWCNT electrode in LiTFSI + TEGDME + MnPc solutions under an Ar or CO_2 atmosphere over a voltage window of 2.3 V to 4.5 V at a current density of 100 mA g^{-1}. (h) Cycling performance of Li-CO_2 cells with and without MnPc in LiTFSI + TEGDME solutions under a specific capacity limit of 500 mAh/g with cycling between 2.3 and 4.5 V at a current density of 50 mA g^{-1}. (i) Electrochemical impedance spectroscopy (EIS) data for the MWCNT electrode in 1 M LiTFSI + TEGDME and 1 M LiTFSI + TEGDME + MnPc solutions after the 10th discharge cycle.

confirming the enhanced reversibility with the MnPc catalyst. Fig. 2**i** presents electrochemical impedance spectroscopy (EIS) data for the Li-CO_2 cells to elucidate the kinetics of charge transfer facilitated by the MnPc catalyst. The semicircles in the Nyquist plot at high frequencies represent the charge transfer resistance at the electrode/electrolyte interface (R_{ct}). Remarkably, the R_{ct} (142 Ω) of the MnPc-containing Li-CO_2 cell was lower than that (240 Ω) of the pristine Li-CO_2 cell, verifying facile charge transfer at the electrode/electrolyte interface upon introduction of the MnPc. The electrochemical results clearly demonstrated that inclusion of MnPc in the electrolyte of a Li-CO_2 cell significantly improved the electrochemical reaction kinetics and cell reversibility and provided a reduction in overpotential.

Some RMs are known to diffuse through a separator and undergo chemical reduction at the Li anode. This process is caused by self-discharge of the RM, which is electrochemically oxidized. To demonstrate whether MnPc self-discharge occurred, the electrochemical behavior of the Li/Li symmetric cell was examined (**Figure S2**). In an Ar atmosphere, the pristine cell showed unstable voltage profiles after 150 h, whereas the cell with MnPc showed a more stable profile after 300 h (**Figure S2a**). It was more pronounced in a CO_2 atmosphere that the pristine Li/Li symmetric cell underwent a short circuit after 39 h; however, the use of MnPc in the Li/Li symmetric cell provided a significantly stable cycling profile lasting 250 h (**Figure S2b**). This implies that MnPc transfers electrons without causing a side reaction with Li metal during cycling. As a result, with MnPc, the negative effects of the Li metal anode were overcome by avoiding the coulombic efficiency degradation caused by self-discharge of the RM.

Li ions and atmospheric CO_2 reactants were converted to Li_2CO_3 and C products in the Li-CO_2 cell during discharge, and the products were reversely decomposed during charging. To gather structural and chemical information on the discharge products, we conducted Fourier transform infrared spectroscopy (FT-IR) at the electrode for different electrochemical states (Fig. 3a). A peak at 1420 cm^{-1} related to COO^- was observed after the discharge process (CO_2 reduction reaction), and the peak disappeared after recharging. To further examine the crystalline features of the discharge products, Fig. 3b shows ex situ XRD results for the electrode collected during different electrochemical states. Distinct peaks associated with a crystalline Li_2CO_3 phase were observed at the discharged electrode, which is consistent with the typical Li_2CO_3 product generated for the Li-CO_2 reaction. The product peaks

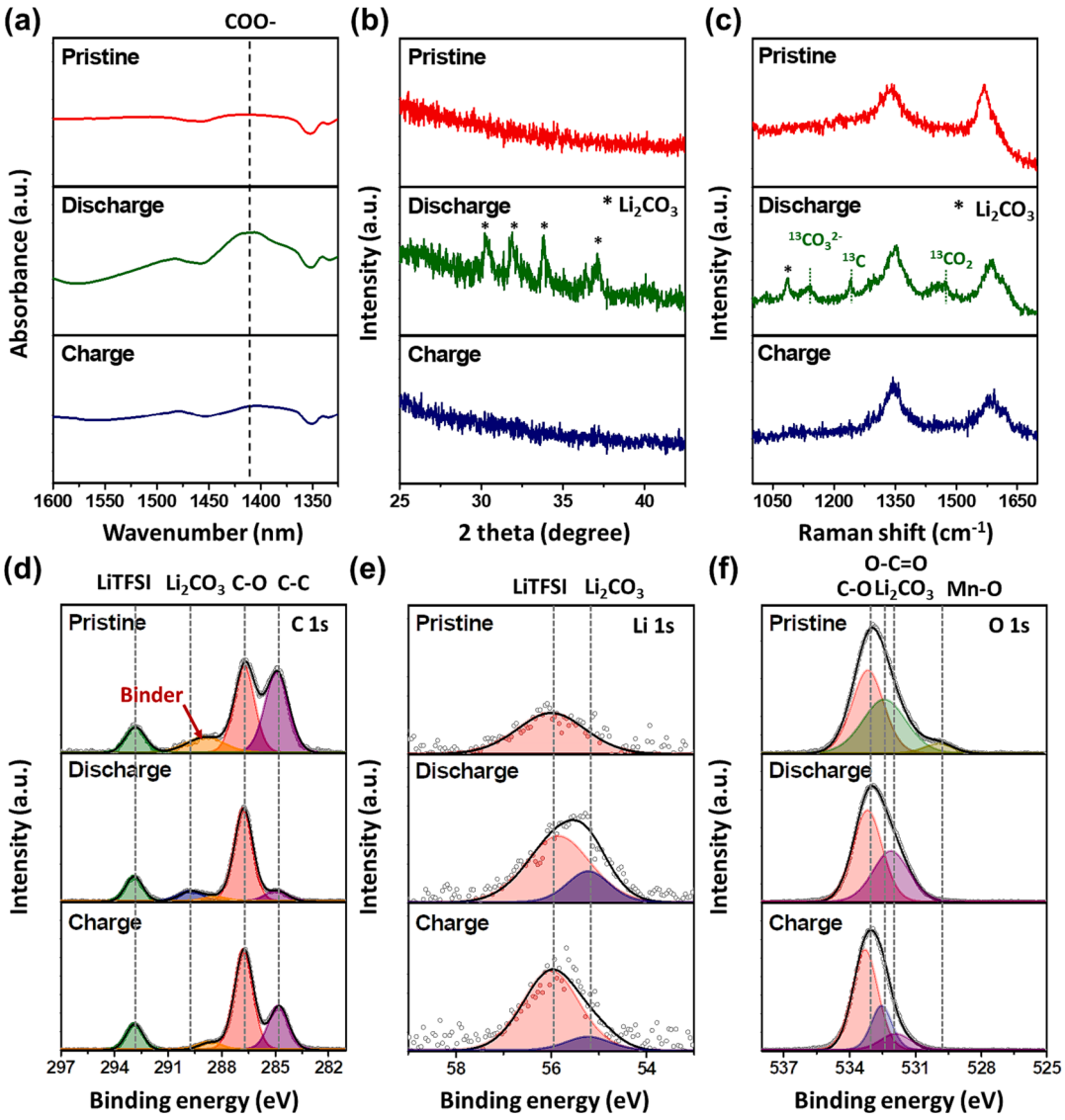

Fig. 3. Ex situ measurements on oxygen electrodes in Li-CO_2 cells. (a) FT-IR results, (b)XRD diffraction patterns of electrodes charged and discharged in Li-CO_2 cells fabricated with and without MnPc in the electrolyte solution. (c) Raman spectra obtained from pristine, once discharged, and once charged electrodes in a Li-CO_2 cell purged with $^{13}CO_2$. Ex situ X-ray photoelectron spectra obtained from pristine, once discharged, and once charged electrodes indicating (d) C 1 s, (e) Li 1 s, and (f) O 1 s binding energies.

disappeared after charging, indicating reversible decomposition without residual crystalline products. The reaction mechanism of the Li-CO_2 cell is still debated, and Li_2CO_3 products could possibly be formed from unexpected side reactions with other carbon sources, such as carbon electrodes or electrolytes[45–51]. To prove that the Li_2CO_3 was produced from the added CO_2 gaseous reactant, we employed isotopically-labelled CO_2 ($^{13}CO_2$) as the purge gas and performed Raman spectroscopy at the electrode during different electrochemical states (Fig. 3c, Figure S3). Broad peaks typically appear at 1350 and 1580 cm^{-1} for the D and G bands for carbon, respectively [52–55]. Peaks originating from the ^{13}C species clearly appeared after discharge, and these were assigned to specific vibrations of $^{13}CO_3^{2-}$ (1100 cm^{-1}), ^{13}C (1240 cm^{-1}), and $^{13}CO_2$ (1420 cm^{-1}) for the case of the Li-CO_2 cell purged with $^{13}CO_2$ [56,57]. On the other hand, the Li-CO_2 cell purged with $^{12}CO_2$ gas did not show peaks related to ^{13}C, which strongly supports our hypothesis that the Li-CO_2 reaction mainly occurs with atmospheric CO_2 rather than in side reactions with other carbon sources. Furthermore, these peaks completely disappeared, confirming reversible decomposition of the discharge products without a residue. Consequently, based on the reversible formation and decomposition of the products ($Li_2^{13}CO_3$ and ^{13}C), we conclude that the CO_2 reduction reaction is $4Li^+ + 3\ CO_2 + 4\ e^- \rightarrow 2\ Li_2CO_3 + C$, with $E_0 = 2.8$ V vs. Li/Li^+. Ex situ X-ray photoelectron spectroscopy (XPS) was used to elucidate chemical bonding and phase changes occurring during cycling (Fig. 3d-f). In the C 1 s XPS spectrum, the pristine, discharged, and charged electrodes showed common peaks corresponding to C-C and C-O bonds (Fig. 3d). The intensities of the C-C peak (284.8 eV) and PVdF binder (288.9 eV) decreased after discharge because discharge products covered the electrode. A peak corresponding to the Li_2CO_3 product on the discharged electrode was detected at 289.5 eV. The Li_2CO_3 product was confirmed by a peak at 55.6 eV (Li_2CO_3) in the Li 1 s spectrum and peaks at 532.5 eV (O-C = O) and 531.7 eV (Li_2CO_3) in the O 1 s spectrum (Fig. 3e and f). After charging, the peaks related to the Li_2CO_3 product entirely disappeared, implying that the reversible Li-CO_2 reaction is mediated by MnPc. Morphological changes of the electrode surface occurring due to product formation and decomposition were studied by ex situ scanning electron microscopy (SEM) (Figure S4). The discharged electrode was covered by the planar products formed in LiTFSI-added TEGDME electrolyte and were reversibly removed to recover the original surface after recharging.

To confirm the experimental findings indicating improved perfor-

mance of Li-CO_2 cells with the MnPc electrolyte catalyst, density functional theory (DFT) calculations were used to study the MnPc-mediated reaction mechanism and the catalytic effect of MnPc for the CRR and CER (Fig. 4). In these calculations, we assumed that MnPc would participate in electrochemical reactions by changing the binding energies of intermediates. We first considered reaction pathways based on the possible intermediates shown in Equations (1) to (14) and Fig. 4a, as in our previous work [46]. The fastest reaction pathway catalyzed by MnPc in the Li-CO_2 cell is drawn with the onset potential U_{DC} for possible intermediate states. In Fig. 4a, the most promising reaction pathways are highlighted in red. Interestingly, the best reaction pathway estimated in this study differed from previously reported reaction pathways seen with an electrocatalyst loaded on the electrode surface[46]. The Li-CO_2 reaction with MnPc generated the Li_2CO_2 intermediate preferentially (ΔG_9) rather than catalyzing direct conversion to $Li_2C_2O_4$ from $LiCO_2$ (ΔG_{11}). Even though the reaction pathways were slightly different, the rate-determining step (RDS) remained the same for the two different pathways. The biggest problem in determining the reaction mechanisms of Li-CO_2 cells is the high charging overpotential caused by the high stability of the Li_2CO_3 product. There are substantial energy drops for the last step (formation of Li_2CO_3, ΔG_{13}) of the discharge process (red color) stemming from the stability of Li_2CO_3 (Fig. 4b and c).

Using the results calculated for the preferred reaction pathway, the reaction energy diagrams for both CRR and CER are represented in Fig. 4**b and c**. In this figure, red colored graphs indicate the discharging process forming the Li_2CO_3 product, and blue colored graphs show the charging process evolving CO_2 gas from the stable Li_2CO_3 product. We also considered another reaction pathway involving the $C_2O_4^{2-}$ intermediate, and this is shown in gray for comparison. However, formation of the $C_2O_4^{2-}$ was more difficult than formation of $LiCO_2$ from CO_2 even though they occurred at the same applied potential. Potential differences (ΔV) between the charging and discharging processes were used to determine the catalytic activity. If the specific system has a small ΔV, which means it only required a small overpotential to charge the Li-CO_2 cell, the small ΔV indicates a better cell performance. While there was not much difference in U_{DC} for both cases, U_C showed an enormous potential difference due to the first evolution step from Li_2CO_3 to $LiCO_2$ (reverse of ΔG_{13}) (Fig. 4**b and c**). Considering the Li_2CO_3 bonding configuration shown in Fig. 4**a and c**, the Mn metal center in MnPc bonded a single O atom in Li_2CO_3, which generated a weak binding energy. We believe that numerous MnPc molecules in the electrolyte actively bonded the CO_2^{*-} radical anions to form Li_2CO_3 and that weak bonding eventually caused ready oxidation of Li_2CO_3 with an overpotential significantly lower than those seen for Li-CO_2 cells without MnPc. The facilitated evolution of Li_2CO_3 was directly confirmed with *in situ* differential electrochemical mass spectrometry (DEMS) by monitoring the CO_2 evolution rates of cells employing MnPc catalysts (Fig. 4**d and e**). The CO_2 gas evolved from Li_2CO_3, and C products should be detected during recharging, based on the CER reaction ($2Li_2CO_3 + C \rightarrow$

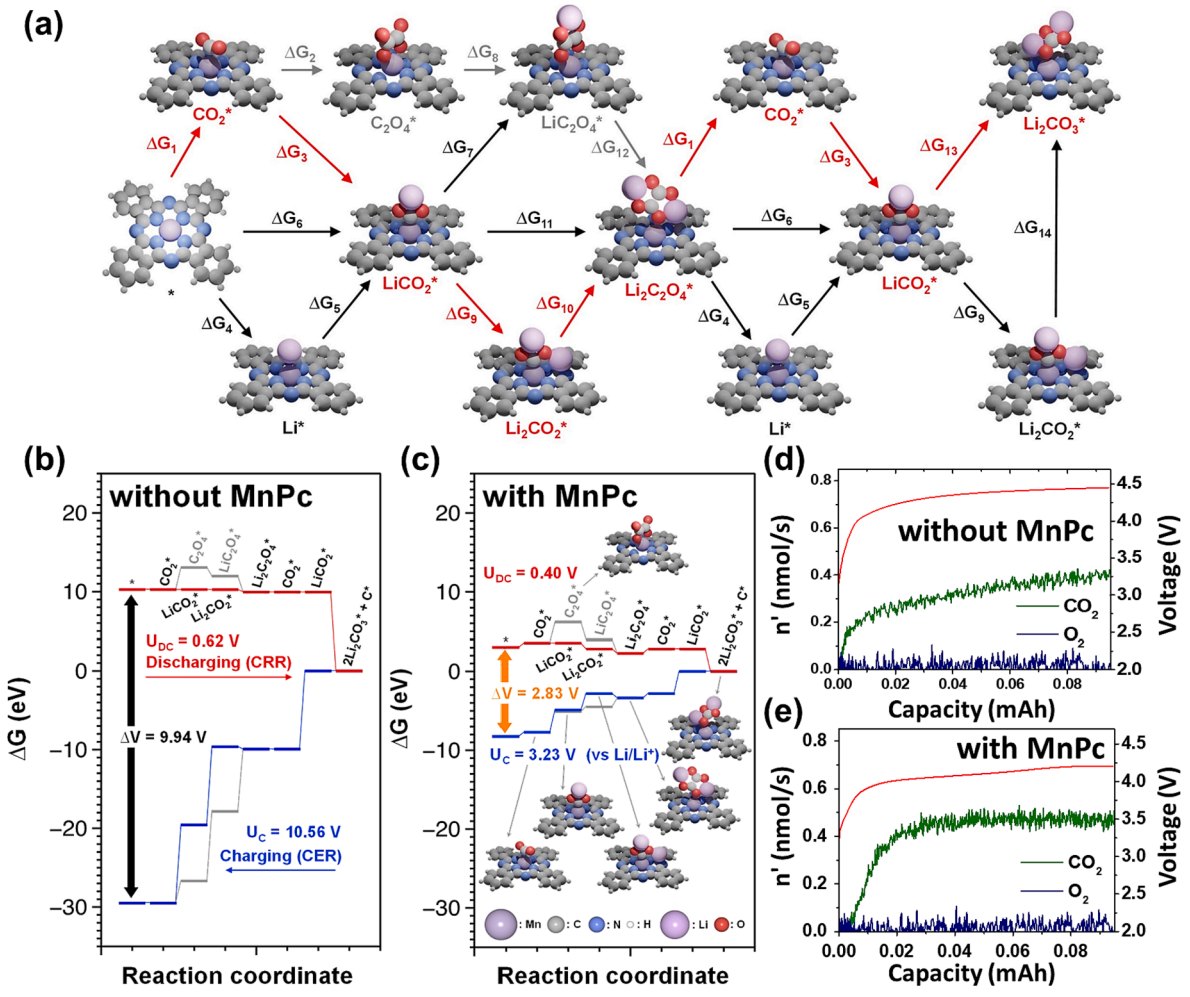

Fig. 4. Reaction pathways and energy diagrams obtained from DFT calculations. (a) Scheme of possible reaction pathways for the CO_2 reduction process; the most promising pathway is highlighted in red; Reaction energy diagram for discharging (red) and charging (blue) with a potential gap (ΔV) (b) without MnPc and (c) with the MnPc complex; *In situ* DEMS results for the rate of CO_2 and O_2 evolution during charging in cells (d) without and (e) with MnPc. (For interpretation of the references to color in this figure legend, the reader is referred to the web version of this article.)

$4Li^+ + 3CO_2 + 4e^-$). The rate of CO_2 evolution for the MnPc-containing Li-CO_2 cell (0.5 nmol/s) was significantly higher than that seen without the MnPc (0.35 nmol/s), which demonstrated excellent CER activity. Interestingly, no O_2 evolution reaction occurred for either Li-CO_2 cell, suggesting that no side reaction except for those of CO_2 species occurred for the CER reaction. These results can be interpreted to indicate that the CER can be achieved with a reduced overpotential by introducing the MnPc electrolyte catalyst.

We successfully demonstrated that the MnPc catalyst dissolved in the electrolyte activated the Li-CO_2 cell reaction with a reduced overpotential and enhanced reversibility. Nevertheless, monitoring the structural and chemical changes of the MnPc catalyst in real time was required to understand the exact role and function of MnPc itself. Therefore, we conducted *in situ* spectroelectrochemical analysis (Fig. 5a, b and Figure S5). Fig. 5a shows the *in situ* ultraviolet–visible (UV–Vis) spectra of MnPc generated during CV scans in 1 M LiTFSi + TEGDME solution under a CO_2 atmosphere, and the spectra were measured over the range 200 nm to 800 nm. MnPc exhibits typical Soret (B) and Q bands in the ranges 300——400 nm and 600——800 nm, respectively, and the Q band absorption of MnPc is related to a $\pi-\pi^*$ transition. The π orbital refers to the highest occupied molecular orbital (HOMO), and the π^* orbital refers to the lowest unoccupied molecular orbital (LUMO) [58,59]. To clearly demonstrate peak changes, a 2D contour plot generated from the 3D profile is shown in Fig. 5b. Before the CRR, the measured spectrum showed the absorption signal for pristine MnPc. During the CRR (discharging) generated by scanning from 3.3 V to 2 V, a new significant peak near 670 nm appeared. This blue-shifted band was associated with a metal-to-ligand charge transfer (MLCT) transition in MnPc. As the discharge reaction occurred, CO_2^{*-} was bound to the Mn atom located in the center of the phthalocyanine ring, and this was accompanied by electron transfer [60–68]. With increasing numbers of CO_2-coordinated MnPc molecules, the intensity of the peak located at 715 nm decreased, and the MLCT band intensity simultaneously increased. As the structure of MnPc reversibly returned to its original state during the CER reaction, the CT band disappeared, and the intensity of the peak for pristine MnPc increased. To test our hypothesis that electrochemically generated CO_2^{*-} radical anions were bound with MnPc, we performed a real-time UV–vis spectrophotometry analysis of the MnPc and monitored the changes in absorbance by simply supplying CO_2 to the electrolyte without applying a reducing potential (Figure S6). There was no significant peak for the CT band after CO_2 purging, verifying that atmospheric CO_2 did not adhere to the transition metal. MnPc tended to bind the electrochemically reduced CO_2^{*-} intermediate generated during electrochemical Li-CO_2 cell reactions. We confirmed these experimental observations with studies of CO_2 (g) and CO_2^{*-} radical anion adsorption on the MnPc complex (Figure S7). CO_2 (g) stayed perfectly flat and exhibited a longer Mn-C bond length (3.5 Å) than the bent CO_2^{*-} radical anion (2.4 Å). From the calculations, we found that CO_2(g) did not change the electronic structure of MnPc due to the weak interaction and claim that only electrochemically reduced CO_2^{*-} radical anions were bound to the MnPc complex to initiate the CRR and change the electronic structure.

We also tried to simulate the absorption spectra via TDHF calculations to compare the simulation and experimental observations and understand the chemical state of the MnPc catalyst corresponding to the blue-shifted absorption peak. As discussed above, we assumed that adsorption of the CO_2^{*-} radical anion would change the absorption spectrum since a shift was observed during the discharge process only; thus, we calculated the absorbance spectra of bare MnPc and MnPc with the CO_2^{*-} radical anion adsorbed to see the differences and prove that our assumption that the absorption spectrum would be changed by CT between the CO_2^{*-} radical anion and the MnPc complex. As a result, we found a blueshift of 30 nm for CO_2^{*-} radical anion adsorption on MnPc (Fig. 5c), which was identical to the experimental observation (Fig. 5a and b). We performed a Bader charge analysis to study CT between the CO_2^{*-} radical anion and the MnPc complex (Fig. 5d) and further analyzed how the excess charge was redistributed onto MnPc on a 2D scale (Fig. 5f) [69–72]. Each color map featuring red and blue colors was exactly matched with the atomic arrangement of the MnPc structure in Fig. 5e. First, 0.56 electrons were transferred to the MnPc complex from the CO_2^{*-} radical anion, and then the excess electron density on the MnPc were redistributed to the ring (red color) near the Mn metal center (blue color). We believe that this charge transfer placed electrons into the HOMO level and induced the blueshift in the absorption spectrum. The bent geometry of the CO_2^{*-} radical anion, which showed an angle of 142.8°, was close to that of the CO_2^{*-} radical anion. The C atom of the asymmetric CO_2^{*-} radical anion was preferentially bonded at the axial coordination site of the Mn center in the MnPc molecule.

3. Conclusions

In summary, we demonstrated the use of MnPc as a homogeneous porphyrin catalysts enabling axial coordination of a CO_2^{*-} radical intermediate in the electrolyte of a Li-CO_2 cell. The Li-CO_2 cell employing MnPc exhibited a 50 % reduction in the overpotential (0.9 V) and long-lasting cycling ability over 80 cycles, which compared favorably to characteristics of the pristine cell (1.8 V, < 30 cycles). A detailed mechanism for charging of the Li-CO_2 cell with the MnPc catalyst proceeded via the sequence $CO_2 \rightarrow LiCO_2 \rightarrow Li_2CO_2 \rightarrow Li_2C_2O_4 \rightarrow Li_2CO_3 +$ C, and the backward reaction was facilitated by the MnPc catalyst, which enabled smaller overpotentials and higher amounts of CO_2 evolved from Li_2CO_3. We examined the real-time structural changes of MnPc molecules during the electrochemical reaction by simulating the absorption spectra and performing charge transfer calculations. The CO_2^{*-} radical anion bent to 142.8°, which was generated during discharging, exhibited bonding to the central Mn atom within the phthalocyanine, and this resulted in charge transfer from the CO_2^{*-} radical anion to the porphyrin ring of MnPc and reversion to the original structure after recharging. Our discovery of the reaction mechanism and the role of the catalyst offers useful information with which to further understand and develop environmental Li-CO_2 battery technology.

4. Experimental Section

Computational Details: GGA-level, spin-polarized density functional theory (DFT) calculations were performed with the Vienna ab initio simulation package (VASP) using a plane wave basis set with a cutoff energy of 400 eV. The revised-Perdew-Burke-Ernzerhof (RPBE) functional was employed to treat the electron exchange and correlation energy [73–75] with the DFT-D3 dispersion correction developed by Grimme [76,77] to consider van der Waals interactions. Since we dealt with inorganic molecules, the Brillouin zone was sampled at the gamma point. The convergence criteria for the electronic and geometric optimizations were 10^{-5} eV and 10^{-2} eV/Å, respectively. We used an isolated manganese phthalocyanine complex (MnPc) molecule structure in this study, in which molecules were centered in a box with a 5 Å gap in all directions. For calculations of the optical absorption spectra, we performed a time-dependent Hartree-Fock (TDHF) calculation [78,79] via a two-step process. First, we calculated the exact band structure with a screened-hybrid exchange functional (HSE06) [80–83] and then evaluated the dielectric function by solving the Casida equation [84].

To calculate the CO_2 reduction (CRR, or discharging) and CO_2 evolution reactions (CER, or charging) for the Li-CO_2 battery, the following reaction steps and intermediates were considered[85–88]:

$$\Delta G_1 = * + CO_2^{*-} \rightarrow CO_2^{*} \quad (1)$$

$$\Delta G_2 = CO_2(g) + CO_2^{*} \rightarrow C_2O_4^{*} \quad (2)$$

$$\Delta G_3 = CO_2^{*} + (Li^+ + e^-) \rightarrow LiCO_2^{*} \quad (3)$$

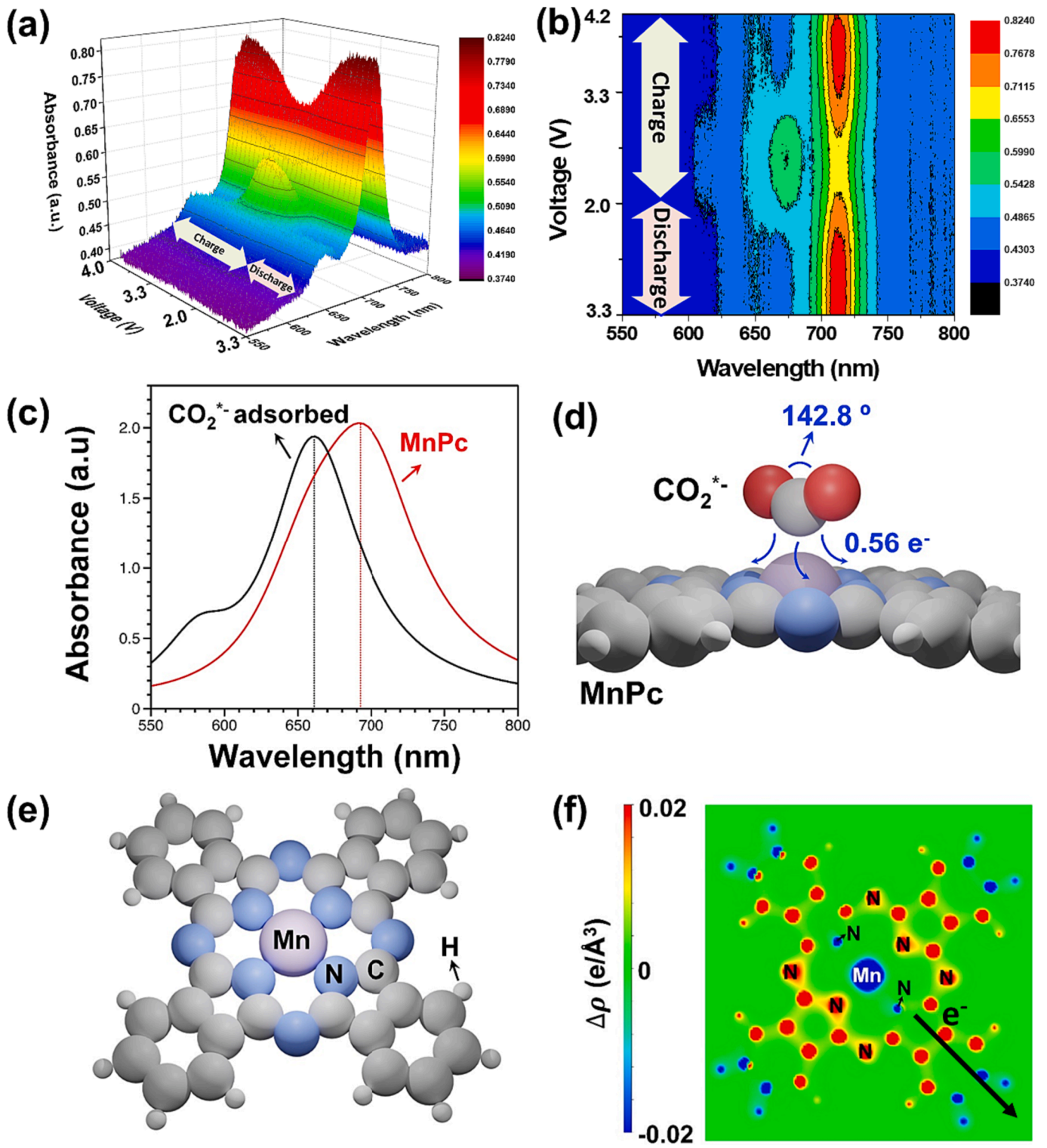

Fig. 5. *In situ* observation of the Mn phthalocyanine molecule in different electrochemical states. Spectroelectrochemical data for 1 M LiTFSI + TEGDME + MnPc; (a) ultraviolet–visible spectrum of 1 M LiTFSI + TEGDME + MnPc; (b) Contour plot showing the absorbance changes of Mn ions during cycling. The spectroelectrochemical tests were performed with a commercial Au honeycomb working electrode and Pt counter electrode over the voltage range −0.97 to 1.23 V versus a Ag pseudoreference electrode in a CO_2 atmosphere. Voltages were converted to reflect a Li/Li^+ reference; (c) Simulated absorption spectra with TDHF on the MnPc complex alone (red) and MnPc with CO_2^{*-} (black); (d) Bending angle of CO_2^{*-} and electron transfer between adsorbed CO_2^{*-} and MnPc; (e) Illustration of the MnPc molecular structure and its atomic positions; (f) 2D mapping of electron redistribution on the MnPc complex after CO_2^{*-} adsorption. The red color represents electron gain, and the blue color represents electron loss. (For interpretation of the references to color in this figure legend, the reader is referred to the web version of this article.)

$$\Delta G_4 = * + (Li^+ + e^-) \rightarrow Li^* \quad (4)$$

$$\Delta G_5 = Li^* + CO_2(g) \rightarrow LiCO_2{}^* \quad (5)$$

$$\Delta G_6 = * + CO_2(g) + (Li^+ + e^-) \rightarrow LiCO_2{}^* \quad (6)$$

$$\Delta G_7 = LiCO_2{}^* + CO_2(g) \rightarrow LiC_2O_4{}^* \quad (7)$$

$$\Delta G_8 = C_2O_4{}^* + (Li^+ + e^-) \rightarrow LiC_2O_4{}^* \quad (8)$$

$$\Delta G_9 = LiCO_2{}^* + (Li^+ + e^-) \rightarrow Li_2CO_2{}^* \quad (9)$$

$$\Delta G_{10} = Li_2CO_2{}^* + CO_2(g) \rightarrow Li_2C_2O_4{}^* \quad (10)$$

$$\Delta G_{11} = LiCO_2{}^* + CO_2(g) + (Li^+ + e^-) \rightarrow Li_2C_2O_4{}^* \quad (11)$$

$$\Delta G_{12} = LiC_2O_4{}^* + (Li^+ + e^-) \rightarrow Li_2C_2O_4{}^* \quad (12)$$

$$\Delta G_{13} = Li_2C_2O_4{}^* + LiCO_2{}^* + (Li^+ + e^-) \rightarrow 2(Li_2CO_3{}^*) + C^* \quad (13)$$

$$\Delta G_{14} = Li_2C_2O_4{}^* + Li_2CO_2{}^* \rightarrow 2(Li_2CO_3{}^*) + C^* \quad (14)$$

The discharging (U_{DC}) and charging (U_C) potentials were calculated from the reaction energy diagrams drawn with the following equation [85–88].

$$\Delta G(U) = \Delta E + \Delta ZPE - T\Delta S + neU \quad (15)$$

where ΔE is the reaction energy obtained from the DFT calculation, ΔZPE is the zero-point energy correction, $T\Delta S$ is the change in entropy, and U is the applied potential. The chemical potential of the lithium cation and the electron pair ($Li^+ + e^-$) under standard conditions was calculated as $\mu^0_{Li(s)} - eU$ by assuming equilibrium at the electrode potential of lithium (0 V vs. Li/Li^+) [89–91]. We calculated the equilibrium potential based on our assumption as 2.7 V (vs. Li/Li^+), and it was 2.8 V (vs. Li/Li^+) in the experiment [12]. There was approximately a 0.1 V deviation from the experiment, which was small enough to predict the activity without any concerns. More importantly, the potential gap between the discharging and charging reactions was a crucial part of determining the performance of the Li-CO_2 battery.

Materials and chemicals: High purity multiwalled carbon nanotubes (SMW100) were donated by Southwest Nanotechnologies. Manganese phthalocyanine, tetraethylene glycol dimethyl ether (TEGDME, 99 %), bis(trifluoromethane) sulfonimide lithium salt (LiTFSI, 99.95 %), poly (vinylidene fluoride) (PVdF, Mw ≈ 180000) and N-methyl-2-pyrrolidone (NMP, anhydrous, 99.5 %) were purchased from Sigma–Aldrich (Korea). Residual moisture was removed from the TEGDME by adding freshly activated molecular sieves (4 Å) into the solvent for 2 weeks.

Preparation of Li-CO2 Cells: The oxygen electrode was fabricated using multiwalled carbon nanotubes (MWCNTs, 90 wt%) and PVdF (10 wt%) dissolved in NMP. The slurry was pasted onto a ∅ 12-mm Ni foam current collector and dried overnight at 80 °C under vacuum conditions. The average slurry mass loading was 0.4 mg per ∅ 12-mm Ni foam. The pristine electrolyte was fabricated using LiTFSI dissolved in TEGDME (1 m) and stirred for 24 h at room temperature. For the MnPc-containing electrolyte, phthalocyanine (0.1 g) and LiTFSI (1 m) were diluted in TEGDME (0.5 mL) and stirred for 24 h in an Ar-filled glovebox to saturate the precursor solution. The supernatant of the saturated MPc electrolyte was used in the single electrolytes. A ∅ 12-mm Li-metal foil was used as the anode, and a glass fiber (Whatman GF/A microfiber filter paper) was used as the separator. Coin cells containing several holes were used for cyclic voltammetry (CV), full discharging–charging, and cycling tests. All cells were assembled in an Ar-filled glovebox. The cells were purged with CO_2 before testing.

Electrochemical characterization: The catalytic activities of the MnPc-containing Li-CO_2 cells were analyzed using cyclic voltammetry (Biologic VSP potentiostat with an impedance function) over the range 2.0–4.5 V and at increasing scan rates up to 100 mV s^{-1}. The charging–discharging tests were performed using a potentiostat/galvanostat (WonATech, Co., Ltd., WBCS3000, Korea) operating at 50 mA g^{-1} in the range 2.3–4.5 V versus Li/Li^+. For the cycling tests, a potentiostat/galvanostat (WonATech, Co., Ltd., WBCS3000 L, Korea) was used at 100 mA g^{-1} with a limiting capacity of 1000 mAh g^{-1} in the same voltage range as the charging–discharging tests. Before the electrochemical tests, the cells were purged with CO_2 gas, and the tests were performed at room temperature.

In situ spectroelectrochemical measurements: Spectroelectrochemical measurements were carried out to monitor the chemical changes of the Mn phthalocyanine molecule occurring during discharge and charge. The electrolytes were transferred into a quartz cuvette with a commercial Au honeycomb electrode (Pine Research Instrumentation, NC, USA). The working electrode was perforated with a honeycomb pattern of holes that allowed light to pass through the electrode. The active surface of the working electrode included a Au coating along the inner walls of the holes. As the light beam from the spectrometer passed through the holes, the beam grazed the walls of each hole. A Pt counter electrode and Pt pseudoreference electrode were used to construct the 3-electrode cell. The electrode potential was controlled with a potentiostat (-0.97–1.23 V vs. SHE) and ultraviolet–vis spectra were collected on a Varian Cary 50 at varying potentials. The electrolytes were purged with dry CO_2 for at least 20 min before each experiment. All potential CV values were calibrated to the Li/Li^+ couple ($E^0 = -3.04$ V).

Time-course ultraviolet–visible spectroscopy: The concentration of Mn phthalocyanine was diluted in LiTFSI/TEGDME (1 M) to generate UV–vis spectra. The CO_2 gas was dissolved by direct purging into the electrolyte for 5 min. Electrolyte solutions (2.5 mL) were added to quartz cuvettes, which were tightly sealed with parafilm, and the UV–vis spectra were measured for 2 h.

Ex situ characterization: The crystal structures and bonding within the electrode samples after cycling were analyzed by X-ray photoelectron spectroscopy (XPS), Raman spectroscopy, and X-ray diffraction (XRD).

The surface morphologies for cycled electrodes were observed using SEM. The samples were cycled by galvanostatic discharging and charging at 50 mA g^{-1}, and each electrode was collected after the initial discharging and charging cycles conducted with no capacity limit. A pristine electrode was dipped into the electrolyte to prepare a control sample. Similar to the pristine electrode, the discharged and charged cells were disassembled in an Ar-filled glovebox.

Declaration of Competing Interest

The authors declare that they have no known competing financial interests or personal relationships that could have appeared to influence the work reported in this paper.

Data availability

Data will be made available on request.

Acknowledgments

This work was supported by a National Research Foundation of Korea (NRF) grant funded by the Korean government (MSIT) (No. RS-2023-00208983, 2022M3J1A1085410, and 2018R1A5A1025224). This work was partly supported by a Korea Institute of Energy Technology Evaluation and Planning (KETEP) grant funded by the Korean government (MOTIE) (20221B1010003B, Integrated High-Quality Technology Development of Remanufacturing Spent Cathode for Low Carbon Resource Recirculation).

Appendix A. Supplementary data

Supplementary data to this article can be found online at https://doi.org/10.1016/j.cej.2023.147141.

References

[1] X. Hu, Z. Li, Y. Zhao, J. Sun, Q. Zhao, J. Wang, Z. Tao, J. Chen, Quasi–solid state rechargeable Na-CO2 batteries with reduced graphene oxide Na anodes, Sci. Adv. 3 (2) (2017) e1602396.

[2] F. Peng, Y. Lim, B. Kim, H.-S. Kim, Z. Li, Z. Zhou, J. Li, W.-H. Ryu, Blooming growth of durable carbon nanotubes bundles from graphite interlayer seeds for free-standing lithium-oxygen battery electrodes, Sustainable Materials Technologies 35 (2023) e00531.

[3] R. Yang, Z. Peng, J. Xie, Y. Huang, R.A. Borse, X. Wang, M. Wu, Y. Wang, Reversible Hybrid Aqueous Li− CO2 Batteries with High Energy Density and Formic Acid Production, ChemSusChem 13 (10) (2020) 2621–2627.

[4] W. Ma, X. Liu, C. Li, H. Yin, W. Xi, R. Liu, G. He, X. Zhao, J. Luo, Y. Ding, Rechargeable Al–CO2 batteries for reversible utilization of CO2, Adv. Mater. 30 (28) (2018) 1801152.

[5] M. Mushtaq, X.-W. Guo, J.-P. Bi, Z.-X. Wang, H.-J. Yu, Polymer electrolyte with composite cathode for solid-state Li–CO2 battery, Rare Met. 37 (6) (2018) 520–526.

[6] N.M. Rezayee, C.A. Huff, M.S. Sanford, Tandem amine and ruthenium-catalyzed hydrogenation of CO2 to methanol, J. Am. Chem. Soc. 137 (3) (2015) 1028–1031.

[7] K. Takechi, T. Shiga, T. Asaoka, A li–o 2/co 2 battery, Chem. Commun. 47 (12) (2011) 3463–3465.

[8] Z. Xie, X. Zhang, Z. Zhang, Z. Zhou, Metal–CO2 batteries on the road: CO2 from contamination gas to energy source, Adv. Mater. 29 (15) (2017) 1605891.

[9] S. Xu, Y. Lu, H. Wang, H.D. Abruña, L.A. Archer, A rechargeable Na–CO 2/O 2 battery enabled by stable nanoparticle hybrid electrolytes, J. Mater. Chem. A 2 (42) (2014) 17723–17729.

[10] X. Xu, W. Shi, P. Li, S. Ye, C. Ye, H. Ye, T. Lu, A. Zheng, J. Zhu, L. Xu, Facile fabrication of three-dimensional graphene and metal–organic framework composites and their derivatives for flexible all-solid-state supercapacitors, Chem. Mater. 29 (14) (2017) 6058–6065.

[11] L. Zhang, W. Liu, W. Shi, X. Xu, J. Mao, P. Li, C. Ye, R. Yin, S. Ye, X. Liu, Boosting lithium storage properties of MOF derivatives through a wet-spinning assembled fiber strategy, Chemistry–A, European Journal 24 (52) (2018) 13792–13799.

[12] Y. Qiao, J. Yi, S. Wu, Y. Liu, S. Yang, P. He, H. Zhou, Li-CO2 electrochemistry: a new strategy for CO2 fixation and energy storage, Joule 1 (2) (2017) 359–370.

[13] H.-S. Kim, J.-Y. Lee, J.-K. Yoo, W.-H. Ryu, Capillary-driven formation of iron nanoparticles embedded in nanotubes for catalyzed lithium–carbon dioxide reaction, ACS Materials Letters 3 (6) (2021) 815–825.

[14] X. Sun, X. Mu, W. Zheng, L. Wang, S. Yang, C. Sheng, H. Pan, W. Li, C.-H. Li, P. He, Binuclear Cu complex catalysis enabling Li–CO2 battery with a high discharge voltage above 3.0 V, Nature, Communications 14 (1) (2023) 536.

[15] J. Xie, Z. Zhou, Y. Wang, Metal–CO2 batteries at the crossroad to practical energy storage and CO2 recycle, Adv. Funct. Mater. 30 (9) (2020) 1908285.

[16] B. Liu, Y. Sun, L. Liu, J. Chen, B. Yang, S. Xu, X. Yan, Recent advances in understanding Li–CO 2 electrochemistry, Energ. Environ. Sci. 12 (3) (2019) 887–922.

[17] X. Li, S. Yang, N. Feng, P. He, H. Zhou, Progress in research on Li–CO2 batteries: Mechanism, catalyst and performance, Chin. J. Catal. 37 (7) (2016) 1016–1024.

[18] A. Khurram, M. He, B.M. Gallant, Tailoring the discharge reaction in Li-CO2 batteries through incorporation of CO2 capture chemistry, Joule 2 (12) (2018) 2649–2666.

[19] Y. Jiao, J. Qin, H.M.K. Sari, D. Li, X. Li, X. Sun, Recent progress and prospects of Li-CO2 batteries: Mechanisms, catalysts and electrolytes, Energy Storage Mater. 34 (2021) 148–170.

[20] J.-Y. Lee, H.-S. Kim, J.-S. Lee, C.-J. Park, W.-H. Ryu, Blood protein as a sustainable bifunctional catalyst for reversible Li-CO2 batteries, ACS Sustainable Chemistry Engineering 7 (19) (2019) 16151–16159.

[21] B. Chen, D. Wang, B. Zhang, X. Zhong, Y. Liu, J. Sheng, Q. Zhang, X. Zou, G. Zhou, H.-M. Cheng, Engineering the active sites of graphene catalyst: From CO2 activation to activate Li-CO2 batteries, ACS Nano 15 (6) (2021) 9841–9850.

[22] Y. Qiao, J. Yi, S. Guo, Y. Sun, S. Wu, X. Liu, S. Yang, P. He, H. Zhou, Li 2 CO 3-free Li–O 2/CO 2 battery with peroxide discharge product, Energ. Environ. Sci. 11 (5) (2018) 1211–1217.

[23] W. Yin, A. Grimaud, I. Azcarate, C. Yang, J.-M. Tarascon, Electrochemical reduction of CO2 mediated by quinone derivatives: implication for Li–CO2 battery, J. Phys. Chem. C 122 (12) (2018) 6546–6554.

[24] H. Wan, Y. Sun, J. Yu, Q. Shi, Y. Zhu, Y. Qian, A chiral salen-Co (II) complex as soluble redox mediator for promoting the electrochemical performance of Li-O2 batteries, Nano Res. 15 (9) (2022) 8101–8108.

[25] W. Yin, A. Grimaud, F. Lepoivre, C. Yang, J.M. Tarascon, Chemical vs electrochemical formation of Li2CO3 as a discharge product in Li–O2/CO2 batteries by controlling the superoxide intermediate, The Journal of Physical Chemistry Letters 8 (1) (2017) 214–222.

[26] S. Xu, S.K. Das, L.A. Archer, The Li–CO 2 battery: A novel method for CO 2 capture and utilization, RSC Adv. 3 (18) (2013) 6656–6660.

[27] B. Lu, B. Chen, D. Wang, C. Li, R. Gao, Y. Liu, R. Mao, J. Yang, G. Zhou, Engineering the interfacial orientation of MoS2/Co9S8 bidirectional catalysts with highly exposed active sites for reversible Li-CO2 batteries, Proceedings of the National Academy of Sciences 120(6) (2023) e2216933120.

[28] Z. Zhang, Q. Zhang, Y. Chen, J. Bao, X. Zhou, Z. Xie, J. Wei, Z. Zhou, The first introduction of graphene to rechargeable Li–CO2 batteries, Angew. Chem. Int. Ed. 127 (22) (2015) 6650–6653.

[29] X. Zhang, Q. Zhang, Z. Zhang, Y. Chen, Z. Xie, J. Wei, Z. Zhou, Rechargeable Li–CO 2 batteries with carbon nanotubes as air cathodes, Chem. Commun. 51 (78) (2015) 14636–14639.

[30] Y. Liu, R. Wang, Y. Lyu, H. Li, L. Chen, Rechargeable Li/CO 2–O 2 (2: 1) battery and Li/CO 2 battery, Energ. Environ. Sci. 7 (2) (2014) 677–681.

[31] X. Hu, Z. Li, J. Chen, Flexible Li-CO2 batteries with liquid-free electrolyte, Angew. Chem. Int. Ed. 129 (21) (2017) 5879–5883.

[32] S. Yang, P. He, H. Zhou, Exploring the electrochemical reaction mechanism of carbonate oxidation in Li–air/CO 2 battery through tracing missing oxygen, Energy Environmental Science 9 (5) (2016) 1650–1654.

[33] L. Su, Z. Zhou, X. Qin, Q. Tang, D. Wu, P. Shen, CoCO3 submicrocube/graphene composites with high lithium storage capability, Nano Energy 2 (2) (2013) 276–282.

[34] Y. Hou, J. Wang, L. Liu, Y. Liu, S. Chou, D. Shi, H. Liu, Y. Wu, W. Zhang, J. Chen, Mo2C/CNT: an efficient catalyst for rechargeable Li–CO2 batteries, Adv. Funct. Mater. 27 (27) (2017) 1700564.

[35] K. Baek, W.C. Jeon, S. Woo, J.C. Kim, J.G. Lee, K. An, S.K. Kwak, S.J. Kang, Synergistic effect of quinary molten salts and ruthenium catalyst for high-power-density lithium-carbon dioxide cell, Nat. Commun. 11 (1) (2020) 1–9.

[36] H.-G. Wang, Q. Wu, L. Cheng, L. Chen, M. Li, G. Zhu, Porphyrin-and phthalocyanine-based systems for rechargeable batteries, Energy Storage Mater. (2022).

[37] W.-H. Ryu, F.S. Gittleson, J.M. Thomsen, J. Li, M.J. Schwab, G.W. Brudvig, A. D. Taylor, Heme biomolecule as redox mediator and oxygen shuttle for efficient charging of lithium-oxygen batteries, Nat. Commun. 7 (1) (2016) 12925.

[38] H.-S. Kim, B. Kim, H.-D. Lim, W.-H. Ryu, Self-Oxygenated Blood Protein-Embedded Nanotube Catalysts for Longer Cyclable Lithium Oxygen-Breathing Batteries, ACS Sustainable Chemistry Engineering 10 (13) (2022) 4198–4205.

[39] H.S. Kim, B. Kim, H. Park, J. Kim, W.H. Ryu, Auto-Oxygenated Porphyrin-Derived Redox Mediators for High-Performance Lithium Air-Breathing Batteries, Adv. Energy Mater. 12 (7) (2022) 2103527.

[40] L. Sun, V. Reddu, A.C. Fisher, X. Wang, Electrocatalytic reduction of carbon dioxide: opportunities with heterogeneous molecular catalysts, Energ. Environ. Sci. 13 (2) (2020) 374–403.

[41] Z. Liang, H.-Y. Wang, H. Zheng, W. Zhang, R. Cao, Porphyrin-based frameworks for oxygen electrocatalysis and catalytic reduction of carbon dioxide, Chem. Soc. Rev. 50 (4) (2021) 2540–2581.

[42] S. Yang, Y. Yu, X. Gao, Z. Zhang, F. Wang, Recent advances in electrocatalysis with phthalocyanines, Chem. Soc. Rev. 50 (23) (2021) 12985–13011.

[43] D. Wang, J. Yang, P. He, H. Zhou, A low-charge-overpotential lithium-CO 2 cell based on a binary molten salt electrolyte, Energy Environmental Science 14 (7) (2021) 4107–4114.

[44] E. Nikoloudakis, I. López-Duarte, G. Charalambidis, K. Ladomenou, M. Ince, A. G. Coutsolelos, Porphyrins and phthalocyanines as biomimetic tools for photocatalytic H 2 production and CO 2 reduction, Chem. Soc. Rev. 51 (16) (2022) 6965–7045.

[45] X. Sun, Z. Hou, P. He, H. Zhou, Recent Advances in Rechargeable Li–CO2 Batteries, Energy Fuel 35 (11) (2021) 9165–9186.

[46] Y.-J. Rho, B. Kim, K. Shin, G. Henkelman, W.-H. Ryu, Atomically miniaturized bi-phase IrO x/Ir catalysts loaded on N-doped carbon nanotubes for high-performance Li–CO 2 batteries, J. Mater. Chem. A 10 (37) (2022) 19710–19721.

[47] N. Feng, B. Wang, Z. Yu, Y. Gu, L. Xu, J. Ma, Y. Wang, Y. Xia, Mechanism-of-Action Elucidation of Reversible Li–CO2 Batteries Using the Water-in-Salt Electrolyte, ACS Appl. Mater. Interfaces 13 (6) (2021) 7396–7404.

[48] M.M. Ottakam Thotiyl, S.A. Freunberger, Z. Peng, P.G. Bruce, The carbon electrode in nonaqueous Li–O2 cells, J. Am. Chem. Soc. 135 (1) (2013) 494–500.

[49] S. Song, W. Xu, J. Zheng, L. Luo, M.H. Engelhard, M.E. Bowden, B. Liu, C.-M. Wang, J.-G. Zhang, Complete decomposition of Li2CO3 in Li–O2 batteries using Ir/B4C as noncarbon-based oxygen electrode, Nano Lett. 17 (3) (2017) 1417–1424.

[50] B.D. McCloskey, A. Speidel, R. Scheffler, D. Miller, V. Viswanathan, J. Hummelshøj, J. Nørskov, A. Luntz, Twin problems of interfacial carbonate formation in nonaqueous Li–O2 batteries, The Journal of Physical Chemistry Letters 3 (8) (2012) 997–1001.

[51] N. Mahne, S.E. Renfrew, B.D. McCloskey, S.A. Freunberger, Electrochemical oxidation of lithium carbonate generates singlet oxygen, Angew. Chem. Int. Ed. 57 (19) (2018) 5529–5533.

[52] A. Chamaani, N. Chawla, M. Safa, B. El-Zahab, One-dimensional glass micro-fillers in gel polymer electrolytes for Li-O2 battery applications, Electrochim. Acta 235 (2017) 56–63.

[53] X. Wang, S. Cai, D. Zhu, Y. Chen, Enhanced electrochemical performance of Li–O 2 battery based on modifying the solid-state air cathode with Pd catalyst, RSC Adv. 5 (107) (2015) 88485–88491.

[54] J. Li, H. Zhao, H. Qi, X. Sun, X. Song, Z. Guo, A.G. Tamirat, J. Liu, L. Wang, S. Feng, Drawing a pencil-trace cathode for a high-performance polymer-based Li–CO2 battery with redox mediator, Adv. Funct. Mater. 29 (11) (2019) 1806863.

[55] Z. Guo, J. Li, H. Qi, X. Sun, H. Li, A.G. Tamirat, J. Liu, Y. Wang, L. Wang, A highly reversible long-life Li–CO2 battery with a RuP2-based catalytic cathode, Small 15 (29) (2019) 1803246.

[56] A. Grishkanich, Y. Chubchenko, M. Kustikova, A. Zhevlakov, L. Konopelko, A. Lunev, I. Noskova, N. Paklinov, Raman and CRDS isotopic resolution spectroscopy

for biomedicine applications, Journal of Physics: Conference Series, IOP Publishing, 2019, p. 012050.
[57] V. Vitkin, A. Polishchuk, I. Chubchenko, E. Popov, K. Grigorenko, A. Kharitonov, A. Davtian, A. Kovalev, V. Kurikova, P. Camy, Raman laser spectrometer: Application to 12C/13C isotope identification in CH4 and CO2 greenhouse gases, Appl. Sci. 10 (21) (2020) 7473.
[58] H. Xu, H. Liu, Analysis of UV-visible spectra of phthalocyanine compounds by quantum chemistry calculation, SPIE, Optical Sensing and Imaging Technologies and Applications, 2018, pp. 83–89.
[59] M. Guina, H. Gong, J. Lu, D. Liu, Optical Sensing and Imaging Technologies and Applications, Proc. of SPIE Vol, 2018, pp. 1084601-1.
[60] E. Trollund, P. Ardiles, M.a.J. Aguirre, S.R. Biaggio, R.C. Rocha-Filho, Spectroelectrochemical and electrical characterization of poly (cobalt–tetraaminophthalocyanine)-modified electrodes: electrocatalytic oxidation of hydrazine, Polygedron 19(22-23) (2000) 2303-2312.
[61] P. Ardiles, E. Trollund, M. Isaacs, F. Armijo, M. Aguirre, Evidence of a stable charge-transfer adduct between 2-mercaptoethanol and cobalt-polytetraaminophthalocyanine, J. Coord. Chem. 54 (3–4) (2001) 183–191.
[62] B. Ortiz, S.M. Park, N. Doddapaneni, Electrochemical and spectroelectrochemical studies of cobalt phthalocyanine polymers, J. Electrochem. Soc. 143 (6) (1996) 1800.
[63] S.i. Mho, B. Ortiz, S.M. Park, D. Ingersoll, N. Doddapaneni, Spectroelectrochemical studies of metallophthalocyanines adsorbed on electrode surfaces, Journal of the Electrochemical Society 142(5) (1995) 1436.
[64] W. Nevin, W. Liu, M. Melnik, A. Lever, Spectro-electrochemistry of cobalt and iron tetrasulphonated phthalocyanines, J. Electroanal. Chem. Interfacial Electrochem. 213 (2) (1986) 217–234.
[65] P. Minor, M. Gouterman, A. Lever, Electronic spectra of phthalocyanine radical anions and cations, Inorg. Chem. 24 (12) (1985) 1894–1900.
[66] A. Lever, S. Pickens, P. Minor, S. Licoccia, B. Ramaswamy, K. Magnell, Charge-transfer spectra of metallophthalocyanines: correlation with electrode potentials, J. Am. Chem. Soc. 103 (23) (1981) 6800–6806.
[67] C.C. Leznoff, H. Lam, S.M. Marcuccio, W.A. Nevin, P. Janda, N. Kobayashi, A. Lever, A planar binuclear phthalocyanine and its dicobalt derivatives, Journal of the Chemical Society, Chemical Communications (9) (1987) 699–701.
[68] W.A. Nevin, M.R. Hempstead, W. Liu, C.C. Leznoff, A. Lever, Electrochemistry and spectroelectrochemistry of mononuclear and binuclear cobalt phthalocyanines, Inorg. Chem. 26 (4) (1987) 570–577.
[69] W. Tang, E. Sanville, G. Henkelman, A grid-based Bader analysis algorithm without lattice bias, J. Phys. Condens. Matter 21 (8) (2009), 084204.
[70] G. Henkelman, A. Arnaldsson, H. Jónsson, A fast and robust algorithm for Bader decomposition of charge density, Comput. Mater. Sci 36 (3) (2006) 354–360.
[71] E. Sanville, S.D. Kenny, R. Smith, G. Henkelman, Improved grid-based algorithm for Bader charge allocation, J. Comput. Chem. 28 (5) (2007) 899–908.
[72] M. Yu, D.R. Trinkle, Accurate and efficient algorithm for Bader charge integration, J. Chem. Phys. 134 (6) (2011), 064111.
[73] J.P. Perdew, K. Burke, M. Ernzerhof, Generalized gradient approximation made simple, Phys. Rev. Lett. 77 (18) (1996) 3865.
[74] Y. Zhang, W. Yang, Comment on “Generalized gradient approximation made simple”, Phys. Rev. Lett. 80 (4) (1998) 890.
[75] B. Hammer, L.B. Hansen, J.K. Nørskov, Improved adsorption energetics within density-functional theory using revised Perdew-Burke-Ernzerhof functionals, Phys. Rev. B 59 (11) (1999) 7413.
[76] S. Grimme, J. Antony, S. Ehrlich, H. Krieg, A consistent and accurate ab initio parametrization of density functional dispersion correction (DFT-D) for the 94 elements H-Pu, J. Chem. Phys. 132 (15) (2010), 154104.
[77] S. Grimme, S. Ehrlich, L. Goerigk, Effect of the damping function in dispersion corrected density functional theory, J. Comput. Chem. 32 (7) (2011) 1456–1465.
[78] S. Albrecht, L. Reining, R. Del Sole, G. Onida, Ab initio calculation of excitonic effects in the optical spectra of semiconductors, Phys. Rev. Lett. 80 (20) (1998) 4510.
[79] M. Rohlfing, S.G. Louie, Electron-hole excitations in semiconductors and insulators, Phys. Rev. Lett. 81 (11) (1998) 2312.
[80] J. Heyd, G.E. Scuseria, M. Ernzerhof, Hybrid functionals based on a screened Coulomb potential, J. Chem. Phys. 118 (18) (2003) 8207–8215.
[81] J. Heyd, G.E. Scuseria, Efficient hybrid density functional calculations in solids: Assessment of the Heyd–Scuseria–Ernzerhof screened Coulomb hybrid functional, J. Chem. Phys. 121 (3) (2004) 1187–1192.
[82] J. Heyd, J.E. Peralta, G.E. Scuseria, R.L. Martin, Energy band gaps and lattice parameters evaluated with the Heyd-Scuseria-Ernzerhof screened hybrid functional, J. Chem. Phys. 123 (17) (2005), 174101.
[83] A.V. Krukau, O.A. Vydrov, A.F. Izmaylov, G.E. Scuseria, Influence of the exchange screening parameter on the performance of screened hybrid functionals, J. Chem. Phys. 125 (22) (2006), 224106.
[84] M.E. Casida, Generalization of the optimized-effective-potential model to include electron correlation: A variational derivation of the Sham-Schlüter equation for the exact exchange-correlation potential, Phys. Rev. A 51 (3) (1995) 2005.
[85] C. Yang, K. Guo, D. Yuan, J. Cheng, B. Wang, Unraveling reaction mechanisms of Mo2C as cathode catalyst in a Li-CO2 battery, J. Am. Chem. Soc. 142 (15) (2020) 6983–6990.
[86] Y. Zhai, H. Tong, J. Deng, G. Li, Y. Hou, R. Zhang, J. Wang, Y. Lu, K. Liang, P. Chen, Super-assembled atomic Ir catalysts on Te substrates with synergistic catalytic capability for Li-CO2 batteries, Energy Storage Mater. 43 (2021) 391–401.
[87] A. Ahmadiparidari, R.E. Warburton, L. Majidi, M. Asadi, A. Chamaani, J. R. Jokisaari, S. Rastegar, Z. Hemmat, B. Sayahpour, R.S. Assary, A long-cycle-life lithium–CO2 battery with carbon neutrality, Adv. Mater. 31 (40) (2019) 1902518.
[88] B. Chen, D. Wang, J. Tan, Y. Liu, M. Jiao, B. Liu, N. Zhao, X. Zou, G. Zhou, H.-M. Cheng, Designing electrophilic and nucleophilic dual centers in the ReS2 plane toward efficient bifunctional catalysts for Li-CO2 batteries, J. Am. Chem. Soc. 144 (7) (2022) 3106–3116.
[89] X. Yu, P.G. Pickup, Recent advances in direct formic acid fuel cells (DFAFC), J. Power Sources 182 (1) (2008) 124–132.
[90] J. Kang, J.-S. Yu, B. Han, First-principles design of graphene-based active catalysts for oxygen reduction and evolution reactions in the aprotic Li–O2 battery, The Journal of Physical Chemistry Letters 7 (14) (2016) 2803–2808.
[91] J.S. Hummelshøj, J. Blomqvist, S. Datta, T. Vegge, J. Rossmeisl, K.S. Thygesen, A. Luntz, K.W. Jacobsen, J.K. Nørskov, Communications: Elementary oxygen electrode reactions in the aprotic Li-air battery, J. Chem. Phys. 132 (7) (2010), 071101.